

# Observation of gyroscopic coupling in a non-spinning levitated ferromagnet

Felix Ahrens<sup>1,2</sup> and Andrea Vinante<sup>1,2,\*</sup>

<sup>1</sup>*Istituto di Fotonica e Nanotecnologie IFN-CNR, 38123 Povo, Trento, Italy*

<sup>2</sup>*Fondazione Bruno Kessler, 38123 Povo, Trento, Italy*

(Dated: April 21, 2025)

A non-spinning permanent ferromagnet is predicted to behave as a gyroscope at sufficiently low frequencies, which can be seen as a manifestation of the Einstein-de Haas effect. This yet unexplored regime has been recently proposed for ultrasensitive precession-based magnetometry and for atomic-like quantum stabilization of a levitated nanomagnet in a static field. Here, we observe signatures of gyroscopic effects in the rotational dynamics of a non-spinning permanent ferromagnet levitated in a superconducting trap. Specifically, we detect spin-rotation coupling between different librational modes, in good agreement with theoretical predictions. From our measurements, we can infer both the intrinsic angular momentum of the levitated magnet and its gyromagnetic  $g$ -factor.

The concept of spin is peculiar to quantum mechanics and has no classical interpretation. In spite of that, it is an established experimental fact that quantum spin corresponds to a real mechanical angular momentum. In particular, as demonstrated by the historical Einstein-de Haas [1] and Barnett [2] experiments, changes in the magnetization of a ferromagnet are associated to changes of its rotational state and vice versa. Both effects are typically observed in soft magnetizable materials. For instance, in the standard Einstein-de Haas setup, a change of magnetization induced in a ferromagnetic sample leads to a change of angular velocity. Here, the exchange of angular momentum between the spins and the lattice is a key ingredient and is still a subject of investigation [3].

An interesting consequence of the Einstein-de Haas equivalence has been recently predicted to hold for a permanent hard ferromagnet, with fixed magnetization with respect to the lattice. That is, the intrinsic angular momentum that arises from fixed magnetization leads to spin-rotation coupling and gyroscopic features in the rigid-body dynamics, even if the ferromagnet is not spinning at all [4–9]. For sufficiently low external torque and slow motion, the ferromagnet will thus exhibit precessional dynamics akin to a spinning top. This regime can be observed only if the induced precession frequency  $\Omega$  is lower than the critical value:

$$\Omega \ll \omega_I = S/I \quad (1)$$

where  $S$  is the intrinsic angular momentum and  $I$  is the moment of inertia, i.e., when the precessional angular momentum  $L = I\Omega$  is smaller than the intrinsic angular momentum  $S$ . The quantity  $\omega_I$  is the so-called Einstein-de Haas frequency of the ferromagnet. For a sphere, the scaling with the radius  $R$  is  $\omega_I \propto 1/R^2$ , which explains why this effect can hardly be observed in macroscopic systems.

If the torque is induced by a weak external magnetic field  $B$ , the ferromagnet will behave as a giant atomic spin, featuring Larmor precession with frequency  $\Omega_L = \gamma_0 B$ , where  $\gamma_0$  is the mean gyromagnetic ratio of the spins [4, 9]. Conversely, if the Larmor precession is higher than the Einstein-de Haas frequency  $\Omega_L > \omega_I$ , the ferromagnet will exhibit classical compass-like librational behavior [10, 11].

The gyroscopic regime may enable ultrasensitive magnetometry in a way similar to atomic spins, with the potential to overcome the standard quantum limits on atomic magnetometers by many orders of magnitude [4, 8, 9]. Furthermore, it has been proposed for testing relativistic frame drag with quantum spin [7]. Remarkably, a levitated ferromagnet can exhibit extreme magnetic field resolution even in the standard librational regime, as recently demonstrated [12]. A different application of the gyroscopic nature of a ferromagnet has been proposed [5, 6], namely that a nanomagnet could be stabilized in an external static field, such as in an Ioffe-Pritchard trap, similarly to an atomic spin. This would represent a violation of the classical Earnshaw theorem [13], which states that a classical magnetic dipole cannot have stable configurations in a static magnetic field.

Here, we present an experiment which directly probes gyroscopic effects in a macroscopic permanent hard ferromagnet. In our experiment the dominant dynamics is still librational, i.e. non-gyroscopic. Nevertheless we can infer gyroscopic spin-rotation coupling between the librational modes as a second order effect by observing elliptical trajectories in the angular motion.

Our experiment consists of a hard ferromagnetic sphere based on a rare earth alloy [14], levitated in a cylindrically symmetrical superconducting trap based on a type-I superconductor. This setup, sketched in Fig. 1a, has been modeled in several previous papers based on the image method [10, 12, 15, 16]. We define  $\mu = -\gamma_0 S$  as the magnetic dipole moment, where  $S$  is the total spin angular momentum and  $\gamma_0$  is the gyromagnetic ratio. The Meissner repulsion between the magnet and the underlying superconductor can be modeled through an image dipole. This repulsion in combination with gravity sets the equilibrium height, while the equilibrium orientation is horizontal, as shown in Fig. 1b. Moreover, while in an ideal cylindrically symmetric setup the dipole is free to rotate on the horizontal plane, in practice the symmetry is always broken, for instance by a residual field with a finite horizontal component. This typically leads to two confined angular modes with very different resonance frequencies [12, 15].

For convenience, let us assume the dipole equilibrium orientation in the  $x$  direction as in Fig. 1a. The magnetic dipole

will then undergo harmonic oscillations along the angles  $\alpha$  and  $\beta$ . We can define harmonic restoring torque for small librations around  $z$  ( $\alpha$  angle) and  $y$  ( $\beta$  angle) as  $T_z = -I\omega_\alpha^2\alpha$  and  $T_y = I\omega_\beta^2\beta$ . Here,  $I$  is the moment of inertia that we assume as isotropic, and  $\omega_\alpha, \omega_\beta$  are resonance frequencies of the librational modes. Experimentally, typical frequencies are of the order of  $f_\alpha = \omega_\alpha/2\pi \sim 100$  Hz and  $f_\beta = \omega_\beta/2\pi \sim 400$  Hz.

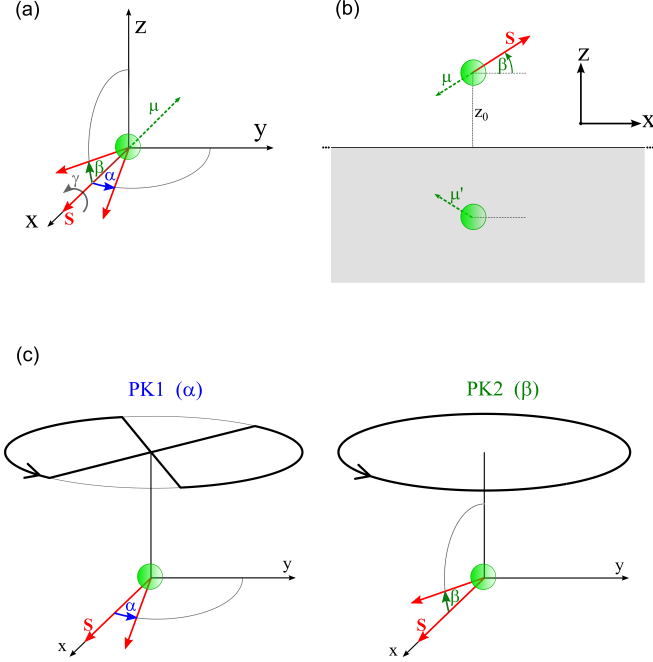


FIG. 1. (a) Model and conventions adopted. A ferromagnet with spin  $\mathbf{S}$  and magnetic moment  $\boldsymbol{\mu} = -\gamma_0\mathbf{S}$  is trapped along the  $x$  axis. It can harmonically librate around  $z$  by an angle  $\alpha$  and around  $y$  by an angle  $\beta$ . (b) Scheme of a ferromagnet above an infinite superconducting plane (gray region) in the Meissner regime. In this implementation, harmonic confinement of the  $\beta$  angle arises naturally due to the interaction with an image dipole  $\boldsymbol{\mu}'$ . (c) Schematic of the pick-up coils used in this work. Coil PK1 is a 8-shape coil optimized for detection of  $\alpha$  motion and ideally insensitive to  $\beta$  motion. Coil PK2 is a circular coil sensitive to  $\beta$  and ideally insensitive to  $\alpha$ .

To assess the contribution of gyroscopic effects we need to solve the most general equation of motion of a ferromagnetic rotor [8, 10]:

$$\begin{aligned}\dot{\mathbf{J}} &= \mathbf{T} \\ \dot{\mathbf{S}} &= \boldsymbol{\Omega} \times \mathbf{S}\end{aligned}\quad (2)$$

Here,  $\mathbf{J} = \mathbf{L} + \mathbf{S}$  is the total angular momentum, with  $\mathbf{L} = I\boldsymbol{\Omega}$  being the kinetic angular momentum, and  $\mathbf{S}$  is the intrinsic angular momentum (which may include both spin and orbital atomic angular momentum),  $\mathbf{T}$  is the torque. While the latter could include any additional torque, here we consider only the restoring torque written above, due to the combination of Meissner and residual fields. Note that the first of Eqs. (2) is stating the conservation of total angular momentum, while the second one arises from the assumption that

the intrinsic spin is rigidly attached to the magnet crystal, i.e.  $\mathbf{S} = S\hat{\mathbf{n}}$  where  $\hat{\mathbf{n}}$  is the unit vector along the easy axis of the magnet. This is a good assumption for a hard ferromagnet, since the internal magnetization dynamics, with characteristic frequencies at several gigahertz, is up to ten orders of magnitude faster than the mechanical motion [4].

The equations can be solved in a general framework [11], but for our purposes it is sufficient to find the solution in the linear approximation for small angles  $\alpha, \beta$  [10]. To this end, we write the total spin as  $\mathbf{S} = S(1, \alpha, \beta)$  and the angular velocity vector as  $\boldsymbol{\Omega} \simeq (0, -\dot{\beta}, \dot{\alpha})$ . Inserting in Eqs. (2) and retaining only linear terms in  $\alpha$  and  $\beta$  we obtain:

$$\begin{aligned}\ddot{\alpha} + \omega_\alpha^2\alpha + \omega_I\dot{\beta} &= 0 \\ \ddot{\beta} + \omega_\beta^2\beta - \omega_I\dot{\alpha} &= 0\end{aligned}\quad (3)$$

In the latter equations we have neglected dissipation. Although the latter is always present in real experiment, we perform measurements over a time shorter than the damping time. We have also neglected the classical rotations around the  $\mathbf{S}$  vector, i.e. we have assumed  $\dot{\gamma} = 0$ , where  $\gamma$  is the rotation angle (see Fig. 1a). We will discuss later the validity of this assumption.

Equations (3) define coupled linear harmonic oscillators with kinetic coupling terms. In the case of well-separated  $\omega_\alpha$  and  $\omega_\beta$ , relevant to our experiment, the solutions of Eqs. (3) describe elliptical oscillations with a dominant axis and a secondary axis. In particular, we can define a quasi- $\alpha$  mode, with  $\alpha$  and  $\beta$  oscillating according to:

$$\begin{aligned}\alpha(t) &= \alpha_0 \sin(\omega_\alpha t), \\ \beta(t) &= g_\alpha \alpha_0 \cos(\omega_\alpha t), \\ g_\alpha &= \frac{\omega_\alpha \omega_I}{\omega_\beta^2 - \omega_\alpha^2}\end{aligned}\quad (4)$$

and similarly a quasi- $\beta$  mode, with  $\alpha$  and  $\beta$  oscillating according to:

$$\begin{aligned}\beta(t) &= \beta_0 \sin(\omega_\beta t), \\ \alpha(t) &= g_\beta \beta_0 \cos(\omega_\beta t), \\ g_\beta &= \frac{\omega_\beta \omega_I}{\omega_\alpha^2 - \omega_\beta^2}\end{aligned}\quad (5)$$

Thus, the  $\pi/2$  phase shift arising from the gyromagnetic coupling in Eqs. (3) implies elliptical trajectories in the  $\alpha - \beta$  plane. The amplitudes on the secondary axes are suppressed by factors  $g_{\alpha,\beta}$  which satisfy  $g_{\alpha,\beta} \ll 1$  as long as  $\omega_I \ll \omega_\alpha, \omega_\beta$ , a condition that holds in our experiment.

In order to experimentally detect the elliptical trajectories expressed by Eqs. (4,5) we need to monitor the motion through at least two independent channels. To this end, in our setup we implement two detection channels with different sensitivity to  $\alpha$  or  $\beta$  motion (labeled as 1 and 2) based on two different superconducting pick-up coils (PK1 and PK2) depicted in Fig. 1c. The coils, connected to two independent

dc SQUIDs, measure the magnetic flux caused by the magnet motion. Both coils are in the same horizontal plane about 2 mm above the magnet and are composed of two loops. The coil PK1 is designed as 8-shape so that it is coupled to  $\alpha$  motion and ideally insensitive to  $\beta$ , while PK2 is designed as a circular coil so that it is coupled to  $\beta$  and ideally insensitive to  $\alpha$ . In practice we achieve an imperfect selectivity, and each coil is typically coupled to the other degree of freedom with a suppression factor of the order of a few percent.

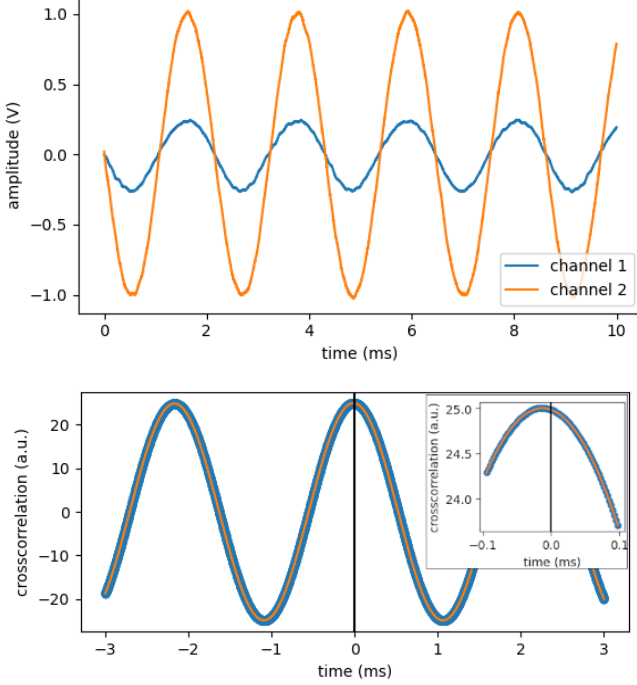


FIG. 2. Representative samples of raw and cross-correlation data. (a) Sample of raw data from channel 1 and channel 2 with quasi- $\beta$  mode excited, over a short time of 10 ms. The frequency of the quasi- $\beta$  mode is 464.4 Hz. (b) Cross-correlation  $C_{12}$  calculated with the same setting of (a) with a total averaging time of 500 ms. In the inset, the cross-correlation is zoomed close to zero time lag. The phase shift with respect to the pure cosine behavior reveals an out-of-phase component as expected from Eqs. (5).

We take imperfections into account by writing the SQUID output voltage in the channels 1 and 2 due to the  $\alpha$  and  $\beta$  motion as:

$$\begin{aligned} V_1(t) &= A\alpha(t) + B\beta(t) \\ V_2(t) &= C\alpha(t) + D\beta(t) \end{aligned} \quad (6)$$

with the only assumptions that by design  $|A| \gg |B|$  and  $|D| \gg |C|$ . The presence of the cross-coupling factor  $C$  implies that when the quasi- $\alpha$  mode is excited, two components will be detected by the secondary channel 2, one in-phase with the main channel 1 due to the cross-coupling  $C$ , and one out-of-phase due to the genuine  $\beta$  motion arising from gyromagnetic coupling through the coupling  $D$ . Specular considerations hold for the quasi- $\beta$  mode. As a representative example, we show in Fig. 2a a sample of raw data from channel 1 and

2 with only the quasi- $\beta$  mode excited, for a microsphere of radius 23.6  $\mu\text{m}$ . At first glance, the two signals are in phase and it is difficult to distinguish the out-of-phase component predicted by Eqs. (5).

In order to unambiguously distinguish an out-of-phase component in the presence of noise, we implement a cross-correlation technique. We define the correlation functions as:

$$C_{ij}(\tau) = \int_0^{t_m} V_i(t) V_j(t + \tau) dt \quad (7)$$

where  $\tau$  is a time lag and the averaging period  $t_m$  is much longer than the oscillation period. Experimentally, the integral is replaced by a sum over the sampled values. We consider two quasi-stationary cases, in which we excite either the quasi- $\alpha$  mode or the quasi- $\beta$  modes to an amplitude much higher than the noise level. For each case the correlation functions is of the form:

$$\begin{aligned} C_{ij}^{(\alpha)}(\tau) &= c_{ij}^{(\alpha)} \cos(\omega_\alpha \tau) + s_{ij}^{(\alpha)} \sin(\omega_\alpha \tau) \\ C_{ij}^{(\beta)}(\tau) &= c_{ij}^{(\beta)} \cos(\omega_\beta \tau) + s_{ij}^{(\beta)} \sin(\omega_\beta \tau) \end{aligned} \quad (8)$$

We extract the in-phase and out-of-phase components  $c_{ij}$ ,  $s_{ij}$  by fitting the experimentally measured correlation functions. Details of the actual numerical procedure are reported in the Supplemental Information [17]. Gyroscopic coupling appears as a non-zero value of the out-of-phase terms  $s_{12}^{(\alpha)}$  and  $s_{21}^{(\beta)}$  while crosstalk through the stray couplings  $B$  and  $C$  will appear in the  $c_{12}$  terms. As an example, Fig. 2b shows the cross-correlation  $C_{12}$  for the same setting of Fig. 2a evaluated over an averaging time  $t_m = 500$  ms. Here, a phase shift is clearly visible in the data, revealing a finite out-of-phase component  $s_{12}$ .

In order to obtain quantitative information on the spin-rotation coupling expressed by the Einstein-de Haas frequency  $\omega_I$ , we combine correlation measurements on the quasi- $\alpha$  mode and the quasi- $\beta$  mode. By means of Eqs. (4, 5, 6, 7, 8) and under the assumptions of partial selectivity  $|A| \gg |B|$  and  $|D| \gg |C|$  and with the further assumption that  $\omega_I \ll \omega_\alpha, \omega_\beta$ , one can show that:

$$r_\alpha r_\beta = \frac{\omega_\alpha \omega_\beta}{(\omega_\beta^2 - \omega_\alpha^2)^2} \omega_I^2 \quad (9)$$

where we have defined:

$$\begin{aligned} r_\alpha &= \frac{s_{12}^{(\alpha)}}{c_{11}^{(\alpha)}} \\ r_\beta &= \frac{s_{21}^{(\beta)}}{c_{22}^{(\beta)}} \end{aligned} \quad (10)$$

The notable feature of Eq. (9) is that it directly connects an experimentally measurable quantity (left-hand side) with a combination of the mode frequencies and the unknown Einstein-de Haas frequency  $\omega_I$ , while it does not contain any

$R$ ( $\mu\text{m}$ )	$M$ (kA/m)	$f_I$ (Hz)	$g$
$31.2 \pm 0.4$	$591 \pm 18$	$0.33 \pm 0.04$	$1.11 \pm 0.14$
$23.6 \pm 0.2$	$675 \pm 20$	$0.62 \pm 0.02$	$1.19 \pm 0.04$
$19.0 \pm 0.2$	$574 \pm 17$	$0.88 \pm 0.05$	$1.10 \pm 0.07$
$18.8 \pm 0.2$	$581 \pm 16$	$0.86 \pm 0.03$	$1.16 \pm 0.04$

TABLE I. Experimental values inferred from the different measurements with different particles. The gyromagnetic frequency  $f_I$  is estimated using the procedure described in the text. The radius  $R$  and magnetization  $M$  are inferred from the observed resonant frequencies of  $\beta$  and  $z$  mode as described in the Supplemental Information. From  $R$  and  $M$  we obtain the mass  $M$  and the magnetic moment  $\mu$ . The  $g$  factor (4th column) is derived from  $\mu$  and  $f_I$ . Note that the 3rd and 4th rows are obtained from measurements on the same particle in two different cooldowns, with significantly different  $\alpha$  mode frequencies.

of the coupling constants  $A$ ,  $B$ ,  $C$  and  $D$ . Therefore, it provides a calibration-free procedure for extracting  $\omega_I$  from the data. Experimentally, we evaluate  $r_\alpha$  and  $r_\beta$  as mean values over many repetitions of the cross-correlation measurement, while their uncertainty is estimated with the mean standard error.

We have performed measurements with four experimental configurations, summarized in Table I. We have used three different microspheres with same material and different radius, and for one of them we have performed two different cooldowns resulting in a very different  $\alpha$  mode frequency. For each setting, we have measured the Einstein-de Haas frequency  $f_I = \omega_I/2\pi$  using the procedure above, which is shown in the third column of Table I. Note that this measurement is calibration-free, so it provides an absolute estimate of the intrinsic angular momentum  $S$  normalized to the moment of inertia  $I$ . For each particle, we determine the radius  $R$  and magnetization  $M$  from the observed mode frequencies. In fact, according to the image method, the frequencies modes  $\beta$  and  $z$  are uniquely determined by  $R$  and  $M$ , as long as the mass density  $\rho$  and the gravity acceleration  $g_0$  are fixed [12]. This procedure is described in detail in the Supplemental Information [17]. From  $R$ ,  $M$  and  $\rho$ , we can derive the mass  $m$ , the magnetic moment  $\mu$  and the moment of inertia  $I$ . The inferred values of  $R$  and  $M$  in the experiment are reported in Table I. In particular, the inferred values of  $R$  are consistent with less precise estimations based on direct optical inspection with a low-magnification microscope during the particle loading process in the trap.

Finally, we can estimate the gyromagnetic  $g$ -factor from the definition:

$$g = \frac{\mu/\mu_B}{S/\hbar} \quad (11)$$

where  $\mu_B$  is the Bohr magneton and  $\hbar$  is the reduced Planck constant. The values of  $g$  inferred from the data, reported in the last column of Table I, are consistent with each other, in agreement with the fact that measurements have been performed with particles made of the same magnetic material.

The numerical values of  $g$  agree reasonably well with the expectations for a rare-earth magnet. The alloy used in this experiment is based on a commercial Nd-Pr-Fe-Co-B alloy. We used this alloy because it is known to maintain magnetization down to cryogenic temperatures, unlike standard NdFeB which may undergo phase transitions. We can reasonably assume that the basic structure is  $\text{Nd}_2\text{Fe}_{14}\text{B}$  with Nd partially replaced by Pr for the rare-earth component, and Fe partially replaced by Co. Taking as reference  $\text{Nd}_2\text{Fe}_{14}\text{B}$ , we estimate a mean effective value for  $g$ :

$$g_{\text{eff}} = \frac{2g_{\text{Nd}}S_{\text{Nd}} + 14g_{\text{Fe}}S_{\text{Fe}}}{2S_{\text{Nd}} + 14S_{\text{Fe}}} = 1.28 \quad (12)$$

where we have used the literature values  $g_{\text{Nd}} = 8/11$ ,  $S_{\text{Nd}} = 9/2\hbar$  for the  $\text{Nd}^{3+}$  ion and  $g_{\text{Fe}} = 2$ ,  $S_{\text{Fe}} = 1/2\hbar$  for Fe [18]. Note again that with  $S$  we mean here the total intrinsic angular momentum, which for rare-earth ions includes both spin or orbital atomic angular momentum. A value of only slightly higher 1.36 is obtained by replacing Nd with Pr. Thus, our experimental estimations are about 10% off the simplest prediction for standard hard ferromagnets based on Nd or Pr.

In spite of the substantial agreement of the experimental data with our spin-rotation coupling model, we need to discuss other mechanisms that could potentially mimic the same results. As shown in the Supplemental Information [17], a classical angular velocity  $\dot{\gamma}$  around the vector  $\mathbf{S}$  would play the same role as the Einstein-de Haas frequency  $\omega_I$ . This is entirely expected on the basis of the Einstein-de Haas equivalence of intrinsic and rotational angular momentum. The coupling between librational modes mediated by  $\gamma$  rotation has been indeed observed recently in levitated nanoparticles [19]. Our SQUID-based detection is blind to  $\gamma$  motion, but we can reasonably assume that it is dominated by thermal noise, since in our setup both librational modes  $\alpha$  and  $\beta$  are thermal [12]. In this case,  $\dot{\gamma}$  is a process with zero mean and standard deviation  $\dot{\gamma}_{\text{rms}} = \sqrt{k_B T/I}$ . For all experimental configurations in Table I we estimate  $\dot{\gamma}_{\text{rms}} < 0.01\omega_I$ . Thus, the effect of  $\dot{\gamma}$  is practically negligible, although it can affect the experimental fluctuations of  $\omega_I$ . Another possible mechanism that could generate a spin-rotation coupling is a deviation from the perfect spherical shape of the particle, implying an anisotropic moment of inertia. However, in this case, the additional mixing between  $\alpha$  and  $\beta$  would not be kinetic, so it would not lead to out-of-phase motion [17].

In conclusion, we have observed elliptical trajectories in the librational oscillations in the  $\alpha - \beta$  plane of an angularly confined levitated hard ferromagnet, witnessed by the appearance of out-of-phase components in the cross-correlation between two independent detection channels coupled to the librational modes, in qualitative agreement with the theoretical model. In particular, the inferred angular momentum and magnetic moment, encoded in the Einstein-de Haas frequency  $f_I$  and the gyromagnetic factor  $g$  factor, agree well with expectations for a rare-earth ferromagnet. To our knowledge, this is the first direct observation of gyroscopic spin-rotation coupling in the dynamics of a macroscopic non-spinning permanent magnet.

In the future, full gyroscopic dynamics should be accessible. For a superconducting trap, a necessary condition is  $\omega_I \gg \omega_\alpha, \omega_\beta$  which requires nanomagnets with radius  $R < 500$  nm. A partial gyroscopic regime where  $\omega_\beta \gg \omega_I \gg \omega_\alpha$ , which would exhibit a modified Larmor precession [8, 11] is, in principle, achievable in the present setup by a proper external compensation of stray fields causing the  $\alpha$  trapping. However, gyroscopic dynamics of a non-spinning ferromagnet is a general effect, which can be, in principle, observed using other platforms, such as Ioffe-Pritchard traps [5, 6], Paul traps [20, 21] or with magnets in free fall [7].

The experimental data used in the analysis will be available in the future to any researcher for purposes of reproducing or extending the analysis.

AV thanks Ben Stickler, Andrejs Cebers and Dmitry Budker for useful discussions. We acknowledge support from the QuantERA II Programme (project LEMAQUME) that has received funding from the European Union's Horizon 2020 research and innovation programme under Grant Agreement No 101017733, and from the Italian Ministry for University and Research within the Italy-Singapore Scientific and Technological Cooperation Agreement 2023-2025.

---

\* anvinante@fbk.eu

- [1] A. Einstein and W. de Haas, Experimental proof of the existence of Ampère's molecular currents, *Koninklijke Akademie van Wetenschappen te Amsterdam Proceedings* **18**, 696 (1915).
- [2] S. Barnett, Magnetization by rotation, *Physical Review* **6**, 239 (1915).
- [3] C. Dornes and et al., The ultrafast Einstein–de Haas effect, *Nature* **565**, 209 (2019).
- [4] D. F. Jackson Kimball, A. O. Sushkov, and D. Budker, Precessing Ferromagnetic Needle Magnetometer, *Physical Review Letters* **116**, 190801 (2016).
- [5] C. Rusconi, V. Pöschhacker, K. Kustura, J. Cirac, and O. Romero-Isart, Quantum spin stabilized magnetic levitation, *Physical Review Letters* **119**, 167202 (2017).
- [6] C. Rusconi, V. Pöschhacker, K. Kustura, J. I. Cirac, and O. Romero-Isart, Linear stability analysis of a levitated nanomagnet in a static magnetic field: Quantum spin stabilized magnetic levitation, *Physical Review B* **96**, 134419 (2017).
- [7] P. Fadeev, T. Wang, Y. Band, D. Budker, P. W. Graham, A. O. Sushkov, and D. F. J. Kimball, Gravity probe spin: Prospects for measuring general-relativistic precession of intrinsic spin using a ferromagnetic gyroscope, *Physical Review D* **103**, 044056 (2021).
- [8] P. Fadeev, C. Timberlake, T. Wang, A. Vinante, Y. B. Band, D. Budker, A. O. Sushkov, H. Ulbricht, and D. F. Jackson Kimball, Ferromagnetic gyroscopes for tests of fundamental physics, *Quantum Science and Technology* **6**, 024006 (2021).
- [9] X. Ni, Z. Zou, R. Lecamwasam, A. Vinante, D. Budker, P. K. Lam, T. Wang, and J. Gong, Microscopic theory of a precessing ferromagnet for ultrasensitive magnetometry, *arXiv:2503.00728* (2025).
- [10] A. Vinante, C. Timberlake, D. Budker, D. F. Jackson Kimball, A. O. Sushkov, and H. Ulbricht, Surpassing the energy resolution limit with ferromagnetic torque sensors, *Physical Review Letters* **127**, 070801 (2021).
- [11] S. Kalia, D. Budker, D. F. J. Kimball, W. Ji, Z. Liu, A. O. Sushkov, C. Timberlake, H. Ulbricht, A. Vinante, and T. Wang, Ultralight dark matter detection with levitated ferromagnets, *Physical Review D* **110**, 115029 (2024).
- [12] F. Ahrens, W. Ji, D. Budker, C. Timberlake, H. Ulbricht, and A. Vinante, Levitated ferromagnetic magnetometer with energy resolution well below  $\hbar$ , *Physical Review Letters* **134**, 110801 (2025).
- [13] R. Bassani, Earnshaw (1805–1888) and passive magnetic levitation, *Meccanica* **41**, 375 (2006).
- [14] Magnequench powder type MQP-S-11-9-20001, see URL: <https://mqitechnology.com/product/mqp-s-11-9-20001/>.
- [15] A. Vinante, P. Falferi, G. Gasbarri, A. Setter, C. Timberlake, and H. Ulbricht, Ultralow mechanical damping with Meissner-levitated ferromagnetic microparticles, *Physical Review Applied* **13**, 064027 (2020).
- [16] A. Vinante, C. Timberlake, and H. Ulbricht, Levitated micro-magnets in superconducting traps: A new platform for tabletop fundamental physics experiments, *Entropy* **24**, 1642 (2022).
- [17] See Supplemental Information at URL for further details on the characterization and modelling of the system.
- [18] K. Buschow and F. de Boer, *Physics of Magnetism and Magnetic Materials* (Kluwer Academic Publishers New York, Boston, Dordrecht, London, Moscow).
- [19] J. A. Zielińska, F. van der Laan, A. Norrman, R. Reimann, M. Frimmer, and L. Novotny, Long-axis spinning of an optically levitated particle: A levitated spinning top, *Physical Review Letters* **132**, 253601 (2024).
- [20] M. Perdriat, C. Pellet-Mary, T. Copie, and G. Hétet, Planar magnetic paul traps for ferromagnetic particles, *Physical Review Research* **5**, L032045 (2023).
- [21] L. Dania, D. S. Bykov, F. Goschin, M. Teller, A. Kasid, and T. E. Northup, Ultrahigh quality factor of a levitated nanomechanical oscillator, *Physical Review Letters* **132**, 133602 (2024).

## SUPPLEMENTAL INFORMATION

### Theoretical model and caveats

Equations (3) in the main text have been derived from Eqs. (2), which state, respectively, the conservation of the total angular momentum and the hard ferromagnet assumption, i.e. the intrinsic angular momentum is rigidly attached to the magnetic particle lattice, so that  $\mathbf{S} = S\hat{\mathbf{n}}$  where  $\hat{\mathbf{n}}$  is a unit vector characterizing the rigid body orientation. For small librational angles  $\alpha$  and  $\beta$ , we can write  $\mathbf{S} = S(1, \alpha, \beta)$ . In addition, we neglect rotations around the  $S$  vector, i.e.  $\dot{\gamma} = 0$ , so for small angles we can write the angular velocity as  $\boldsymbol{\Omega} = (0, -\dot{\beta}, \dot{\alpha})$ . Also, we do not consider dissipation. Finally, we remark that we assume the particle as perfectly spherical and isotropic, allowing us to simplify the tensor of inertia  $I_{ij}$  as a scalar  $I$ .

For the concrete derivation one inserts the second of Eqs. (2) into the first one taking into account that  $\mathbf{J} = I\boldsymbol{\Omega} + \mathbf{S}$  leading to:

$$I\dot{\boldsymbol{\Omega}} + \boldsymbol{\Omega} \times \mathbf{S} = \mathbf{T} \quad (\text{S1})$$

By inserting the specific expressions of  $\mathbf{S}$  and  $\boldsymbol{\Omega}$  above, one finds Eqs. (3) of the main. We now consider two possible refinements of the model. First, we will consider the effect of a finite angular velocity  $\dot{\gamma}$ , and then we will abandon the assumption of isotropic  $I$ .

If the magnet is spinning around the spin axis  $\hat{\mathbf{n}}$  with angular velocity  $\dot{\gamma}$ , the total angular velocity becomes:

$$\boldsymbol{\Omega} = (0, -\dot{\beta}, \dot{\alpha}) + \dot{\gamma}\hat{\mathbf{n}} = (\dot{\gamma}, \dot{\gamma}\alpha - \dot{\beta}, \dot{\gamma}\beta + \dot{\alpha}) \quad (\text{S2})$$

By inserting this expression into Eq. (S1) one finds:

$$\begin{aligned} \ddot{\alpha} + \omega_\alpha^2 \alpha + (\omega_I + \dot{\gamma})\dot{\beta} &= 0 \\ \ddot{\beta} + \omega_\beta^2 \beta - (\omega_I + \dot{\gamma})\dot{\alpha} &= 0 \end{aligned} \quad (\text{S3})$$

We can thus see that a classical angular velocity  $\dot{\gamma}$  plays the same role of the Einstein-de Haas frequency  $\omega_I$ . This can be seen again as a statement of equivalence between intrinsic and rotational angular momentum, i.e. the Einstein-de Haas effect. However, we do not expect  $\dot{\gamma}$  to play a significant role in our experiment. In fact, in the thermal noise limit  $\dot{\gamma}$  is a stochastic process with zero mean and standard deviation  $\dot{\gamma}_{\text{rms}} \ll \omega_I$ . This justifies the initial assumption  $\dot{\gamma} = 0$ .

Next, we will assess the effect of a possible deviation from sphericity. This is a relevant point, since the experimental effect measured in the experiment is quite tiny. A non-isotropic moment of inertia is represented by a symmetric tensor  $I = I_{ij}$ , where  $i, j$  denote the three axis  $x, y, z$ . We write Eq. (S1) taking into account that  $I$  in the first term on the left-hand side is a tensor, which leads to the appearance of additional terms. For simplicity we maintain all other assumptions of the main text, i.e. we set  $\dot{\gamma} = 0$ ,  $\mathbf{S} = S(1, \alpha, \beta)$ ,  $\boldsymbol{\Omega} = (0, -\dot{\beta}, \dot{\alpha})$ . For consistency, the restoring torque is now

given by  $\mathbf{T} = (0, I_{yy}\omega_\beta^2, -I_{zz}\omega_\alpha^2)$ . Eventually we find the following new equations:

$$\begin{aligned} \ddot{\alpha} + \omega_\alpha^2 \alpha + \omega_{I\alpha}\dot{\beta} - \epsilon_\alpha\ddot{\beta} &= 0 \\ \ddot{\beta} + \omega_\beta^2 \beta - \omega_{I\beta}\dot{\alpha} - \epsilon_\beta\ddot{\alpha} &= 0 \end{aligned} \quad (\text{S4})$$

Here, we have defined the Einstein-de Haas frequencies for each mode  $\omega_{I\alpha} = S/I_{zz}$  and  $\omega_{I\beta} = S/I_{yy}$ . Moreover, we have defined the new cross-coupling factors  $\epsilon_\alpha = I_{yz}/I_{zz}$  and  $\epsilon_\beta = I_{yz}/I_{yy}$ , which are associated with the non-diagonal element  $I_{yz}$  of the inertia tensor. The latter is in general different from zero, unless the axes  $y$  and  $z$  coincide with the principal axis of the inertia ellipsoid.

We can draw two main conclusions from Eqs. (S4). First, additional mixing terms appear between  $\alpha$  and  $\beta$  motion, associated with the factors  $\epsilon_\alpha$  and  $\epsilon_\beta$ . However, the coupling associated with these terms is not kinetic, as it appears on the second derivative of the secondary angle, rather than on the first derivative. As a consequence, it does not lead to any out-of-phase component in the secondary detection channel. The gyroscopic coupling responsible for the elliptical trajectories, which is the main output of the experiment, is therefore unaffected. The second relevant point is that the two modes feature different Einstein-de Haas couplings. Since our experimental protocol combines the factors  $r_\alpha$  and  $r_\beta$  inferred from measurement of the quasi- $\alpha$  and quasi- $\beta$  modes, the quantity that we actually extract from the data is the geometric mean:

$$\omega_I = (\omega_{I\alpha}\omega_{I\beta})^{\frac{1}{2}} = \frac{S}{(I_{yy}I_{zz})^{\frac{1}{2}}}. \quad (\text{S5})$$

Deviations from sphericity of our ferromagnetic spheres are estimated to be of the order of 1% or smaller, so their impact on the experiment will be smaller than the error bar on  $\omega_I$ . This justifies the assumption of sphericity and isotropic moment of inertia.

### Methods

The micromagnetic spheres used in the experiment are picked from a commercial powder [11] and are made of a rare-earth compound based on neodymium-iron-boron with nominal composition Nd-Pr-Fe-Co-Ti-Zr-B. The trap is a cylindrical hole made in a bulk piece of Pb (purity 99.95%), with a hemispherical bottom. The radius of the hole and the hemispherical bottom is  $R = 2.5$  mm. For each run of the experiment, an individual micromagnet is selected, magnetized inside an NMR magnet with a field of 10 T, and finally placed at the bottom of the trap using a micromanipulator. The two pick-up coils are made of three turns of 100  $\mu\text{m}$  diameter NbTi wire, wound on a polymeric coil holder. The radius of each coil is  $r_{\text{pk}} = 2$  mm and the vertical position is approximately 2 mm from the bottom of the trap. Each coil is connected to the input coil of a dc SQUID (Magnicon two-stage SQUID current sensor) forming a superconducting loop, as shown in

Fig. S1. Onto the same coil holder we have wound two additional coils that can be connected to an external line. We used these lines to apply an external magnetic field in the trap.

Trap and SQUIDs are housed in a vacuum chamber that is inserted in a liquid helium dewar. The chamber can be filled with helium gas at variable pressure. The dewar is placed on top of an active vibration-isolation platform. At the operating liquid helium bath temperature  $T = 4.18$  K, the micromagnet spontaneously levitates due to the Meissner effect, featuring normal modes corresponding to translational and rotational motion. We detect five normal modes of the levitated microsphere, three translational ( $x, y, z$ ) and two librational ( $\alpha, \beta$ ). The modes can be easily singled out, because their quality factors scale inversely with the gas pressure  $P$ . Specific modes are identified by comparison with analytical and finite element modeling [9,12]. In particular, the modes  $z$  and  $\beta$  are almost entirely determined by the Meissner repulsion. This allows an in-situ determination of the magnetic sphere parameters by comparison with analytical models, as discussed in the next section. Measurements are performed at a pressure  $P \sim 10^{-2}$  mbar, which leads to a damping time of normal modes of the order of 20 seconds. This relatively high gas damping ensures that the librational modes are dominated by thermal noise [9].

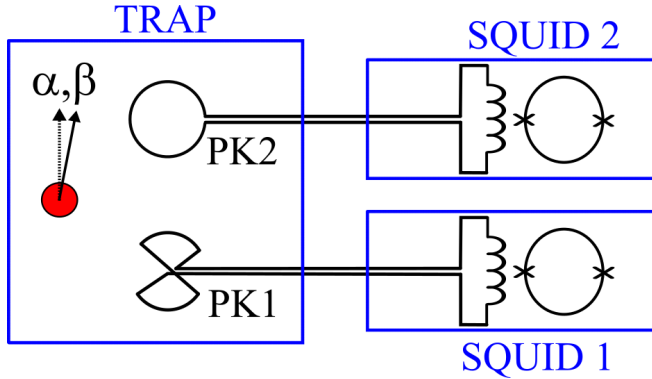


FIG. S1. Measurement scheme showing explicitly the levitated micromagnet and the two pick-up coils inside the superconducting lead trap. Each coil forms a superconducting loop with the input coil of a dc SQUID, hosted in a separate superconducting shield. The librational motion of the micromagnet couples a magnetic flux into each pick-up coil, which is measured by the dc SQUID via the superconducting loop.

The two SQUIDs are operated by a single multichannel readout electronics operated in flux-locked loop (Magnicon XXF-1). We use the same parameter setting for each channel, in order to minimize differential delays. In some measurements, we bandpass filter the data around the desired librational mode ( $\alpha$  or  $\beta$ ) to clean the data from the translational modes. We carefully tune the filters on each channel to provide the same phase shift at the measurement frequency. Using a lock-in amplifier, we check that the differential phase delay between the two channels is always smaller than 0.01 degree.

Data acquisition for the determination of  $\omega_I$  proceeds as follows. First we excite the relevant mode (quasi- $\alpha$  or quasi- $\beta$ ) at an estimated amplitude of the order of  $10^{-2}$  rad, then the signals from the two SQUIDs are acquired by a two-channel digital oscilloscope (Picoscope 4000). Data sets of a length ranging between 0.2 – 1 s depending on the mode frequency, corresponding to a number of periods in the range  $\sim 25 - 300$ , are acquired and stored for post-processing data analysis. The length of each data set is much smaller than the damping time, allowing us to neglect dissipation in the model.

### Determination of micromagnet parameters

We determine the radius  $R$  and the magnetization  $M$  of the ferromagnetic microsphere in situ from the resonance frequencies of the  $z$  and  $\beta$  modes, which are determined by the combination of gravity with Meissner repulsion from the bottom of the trap. The procedure has been extensively discussed in Ref. [9]. We summarize here the main points.

The problem of a magnet above an infinite superconducting plane can be modeled analytically using the image method. The potential energy is a function of the vertical coordinate  $z$ , the azimuthal angle  $\beta$ , the parameters of the sphere (radius  $R$ , density  $\rho$ , magnetization  $M$ ) and the gravitational acceleration  $g_0$ .

Our trap is a cylindrical hole with a hemispherical bottom, so it is quite different from an infinite plane. Infinite plane solutions are still quite reliable, as the equilibrium height of the particle (typically  $z_0 \approx 200 - 300 \mu\text{m}$ ) is much smaller than the radius of the trap width ( $a = 2.5$  mm). An even better approximation is provided by the image method for a spherical cavity inside a superconductor [30]. In this case the potential energy can be written as:

$$U = \frac{\mu_0 \mu}{4\pi} \frac{a^5}{(a^2 + r^2)(a^2 - r^2)^3} \left( 1 + \frac{a^2}{r^2} \sin^2 \beta \right) + mg_0 z. \quad (\text{S6})$$

Here,  $r$  is the distance of the magnet center from the hemispherical trap center,  $m = \rho V$  is the mass and  $\mu = MV$  the magnetic dipole moment, where  $M$  is the magnetization and  $V = 4\pi/3 R^3$  is the magnet volume. The equilibrium height from the bottom  $z_0 = a - r$  and the equilibrium angle  $\beta$  can be calculated numerically by minimizing  $U$ . As in the infinite-plane case, the equilibrium orientation is in the horizontal plane  $\beta = 0$ .

Resonance frequencies of  $z$  and  $\beta$  modes can be calculated numerically from the second derivatives of  $U$ , the mass  $m$  and the moment of inertia  $I = 2/5 m R^2$ :

$$f_z = \frac{1}{2\pi} \sqrt{\frac{1}{m} \frac{\partial^2 U}{\partial z^2} \bigg|_{z=z_0, \beta=0}} \quad (\text{S7})$$

$$f_\beta = \frac{1}{2\pi} \sqrt{\frac{1}{I} \frac{\partial^2 U}{\partial \beta^2} \bigg|_{z=z_0, \beta=0}} \quad (\text{S8})$$



In our experiment, we consider as unknown parameters the radius  $R$  and the magnetization  $M$ . We consider known, within a systematic uncertainty, all other parameters. Gravitational acceleration at our site in Trento (Italy) can be determined from gravitational reference data as  $g_0 = 9.8067 \text{ m/s}^2$  with negligible uncertainty. The density of the material is provided by the manufacturer at room temperature as  $\rho = 7430 \text{ kg/m}^3$ . We assume a conservative relative uncertainty of 5% to take into account thermal contractions and possible surface oxidation. The trap radius is taken as 2.5 mm as by design, with a relative uncertainty of 10% taking into account machining accuracy.

The resonance frequencies of  $z$  and  $\beta$  modes can be measured with very high precision, for instance by ring-down measurements. We take, however, as a major source of uncertainty the reproducibility of the frequency across different cooldowns, which is of the order of 1%, likely due to non-reproducibility of the residual magnetic field in the trap. In addition, as discussed in Ref. [9], we apply a small correction to the  $\beta$  mode frequency:

$$f_\beta \rightarrow \sqrt{f_\beta^2 - f_\alpha^2}. \quad (\text{S9})$$

in order to remove the effect of the spurious field which determines the  $\alpha$  mode

For each magnetic particle used in the experiment, we use the values of  $f_z, f_\beta, \rho, a, g_0$  with their respective uncertainty, and we numerically solve Eqs. (S7,S8) for  $M$  and  $R$  taking into account error propagation. The values of  $R$  and  $M$  are shown in the first two columns of Table 1. From  $M$  and  $R$  we can estimate all other parameters, such as volume  $V$ , mass  $m$ , and moment of inertia  $I = 2/5 m R^2$ .

As noted in the main text, the in situ estimations of  $R$  are in agreement with less precise direct estimations based on optical inspection.

### Data analysis and experimental uncertainties

Each data set consists of a pair of time traces, referring to channel 1 and channel 2, simultaneously sampled with a sampling time  $dt$  over a time  $T$ , for a total number of samples  $N = T/dt$ . Both signals contain the excited librational mode ( $\alpha$  or  $\beta$ , in the following we omit for simplicity the index  $\alpha$  or  $\beta$ ) oscillating at frequency  $\omega$ .  $T$  and  $dt$  are chosen so that  $dt \ll 2\pi/\omega \ll T$ .

For a given pair of channel  $i, j \in 1, 2$  we calculate the correlation (autocorrelation if  $i = j$ , cross-correlation if  $i \neq j$ ) as:

$$C_{ij}(k dt) = \sum_n V_i[(n+k) dt] V_j(n dt) \quad (\text{S10})$$

where  $\tau = k dt$  and  $k \in (-N, N)$  is the time delay.

The dataset  $C_{ij}(\tau)$  is then fitted by the function:

$$f(\tau) = A_0 (1 - A_1 |\tau|) \cos(\omega\tau + \varphi) \quad (\text{S11})$$

with  $A_0, A_1, \omega, \varphi$  free fitting parameters. The envelope  $1 - A_1 |\tau|$  is an artifact that arises from the definition of correlation. Specifically, the overlap between the two waveforms depends on the delay, so that the number of terms in the sum is  $N - |k|$ . Thus, the correlation has a natural envelope of the form  $1 - |k| dt / T$  and vanishes for  $|k| \geq N$ . We find no substantial differences in the fitting parameters by fitting over the whole domain of the correlation or by restricting the fit to a small interval of the order of a few oscillation periods around zero delay.

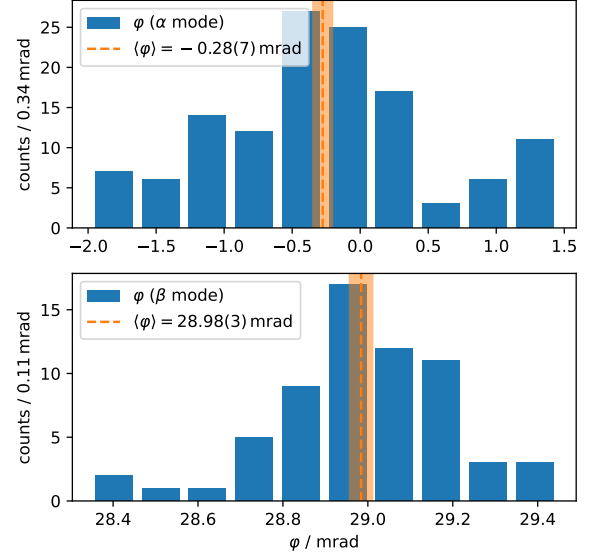


FIG. S2. Distribution of the phase  $\varphi$  obtained from fitting 128 (64) correlated  $\alpha$  mode ( $\beta$  mode) time traces with Eq. (S11) for one of the four measurement runs reported in the paper. The distributions' mean values are indicated with their statistical error.

Following the definition given in Eq. (8) of the main text, we calculate  $c_{ij}$  and  $s_{ij}$  as:

$$\begin{aligned} c_{ij} &= A_0 \cos(\varphi) \\ s_{ij} &= -A_0 \sin(\varphi) \end{aligned} \quad (\text{S12})$$

As a crosscheck we have verified that the out-of-phase component of the auto-correlation of each channel,  $s_{ii}$ , is zero within the error bar.

The  $r_i$  factors ( $i = \alpha, \beta$ ) for the individual data set is then calculated from the definition given in Eq. (10) as the ratio of the out-of-phase cross-correlation to the auto-correlation of the main channel. Note that from the definition, the  $r_i$  factor is independent of the actual amplitude  $A_0$ , which can vary over different data sets.

We repeat the same analysis on all acquired pairs of waveforms. We estimate the mean value of  $r_i$ , and we use the standard deviation of the mean as experimental uncertainty. An example of a fit is shown in Fig. 2 of the main paper, while in



Fig. S2 we show an example of the distribution of the phase  $\varphi$  extracted by fitting 128 (64) correlated  $\alpha$  mode ( $\beta$  mode) time traces with Eq. (S11). The data refer to the particle with radius  $R = 31.2 \mu\text{m}$  in Table I. The mean value  $\langle\varphi\rangle$  and its statis-

tical error, which are used for the subsequent data analysis, are highlighted. We repeat the same procedure by exciting the other mode, and finally, using Eq. (9) we can extract the Einstein-de Haas frequency  $\omega_I$ .